IEEE Access
Multidisciplinary ⋮ Rapid Review ⋮ Open Access Journal

Received 5 April 2024, accepted 2 May 2024, date of publication 6 May 2024, date of current version 14 May 2024.

Digital Object Identifier 10.1109/ACCESS.2024.3397249

RESEARCH ARTICLE

Characteristic Modes Analyses for Misalignment in Wireless Power Transfer System

FERDAOUS ABDERRAZAK[1,2], (Student Member, IEEE), EVA ANTONINO-DAVIU[1], (Member, IEEE), LARBI TALBI[2], (Senior Member, IEEE), AND MIGUEL FERRANDO-BATALLER[1], (Life Senior Member, IEEE)

[1]Institute of Telecommunications and Multimedia Applications (iTEAM), Universitat Politècnica de València, 46022 Valencia, Spain
[2]Department of Computer Science and Engineering, University of Quebec in Outaouais, Gatineau, QC J8X 3X7, Canada

Corresponding author: Ferdaous Abderrazak (abdf12@uqo.ca)

This work has been funded by the Spanish Ministry of Science, Innovation and Universities (Ministerio de Ciencia, Innovación y Universidades) under project PID2022-136869NB-C33.

ABSTRACT This paper presents a novel method for assessing misalignment scenarios in Magnetically Coupled Resonant Wireless Power Transfer (MCR-WPT) system through measurements using Characteristic Modes Analysis (CMA). Based on the metric parameters of Characteristic Modes (CMs), including resonant frequencies, magnetic field plots, and current distributions, the dominant CM is identified. Its impact on the system's total power is evaluated and compared with the system's behavior in proximity to resonance. To establish a comprehensive and concise reference delineating the applicability of CMA in the field of Wireless Power Transmission, this contribution conducts a detailed investigation about the various types of unexpected misalignments between the Transmitting (Tx) and the Receiving (Rx) coils due to typical movement of the device or the user from both analytical and experimental perspectives. Besides, the various misalignment scenarios were systematically and progressively explored, accounting for both minor and significant degrees of variation. The proposed MCR-WPT system consists of two identical loops characterized by a singular turn, a radius R of 0.0625λ and a width w of $0.025R$. Notably, results based on CMA guided by The Coupled Mode Theory (CMT) demonstrate a great affinity with the measurements of the fabricated prototypes. Consequently, this marks the inaugural confirmation of CMA's applicability in the field of Wireless Power Transmission, which opens avenues for improving PTE using previous research findings deploying principles of selective excitation through CMA concepts.

INDEX TERMS Characteristic modes, coupled mode theory, coupling, misalignment, power efficiency, Qi standard, magnetically coupled resonators, wearable electronics, wireless power transfer.

I. INTRODUCTION

Wireless Power Transfer (WPT) has been a cornerstone of the scientific and industrial fields of our society over the past 40 years. WPT is emerging as the solution for delivering cost-effective wireless charging to a wide range of modern technologies, such as 6G Internet of Everything Mobile Networks [1], portable equipment [2], wearable electronics [3], embedded medical apparatus [4], Electrical Vehicles charging [5] and consumer electronics in general [6]. Depending upon the specific application, WPT technology is developed toward two major directions depending on the transmission distance. As such, near-field (NF) techniques are directed to typical transmissions from a few millimeters to a few meters [1], [5], while far-field (FF) techniques point equal or greater range of coverage of typical personal area network [7], [8]. With regards to these, the WPT in the NF is reaching a mature stage for domestic and industrial applications since its implementation is extremely efficient in terms of energy conversion and highly simple in the context of fabrication. Despite inductive coupling via Magnetically Coupled Resonant Wireless Power Transfer (MCR-WPT) systems being the most popular, its short transmission range and sensitivity to misalignment are two major limitations that introduce significant drawbacks into the Power Transfer Efficiency (PTE) [9], [10].

The associate editor coordinating the review of this manuscript and approving it for publication was Diego Masotti.

TABLE 1. Summary of existing survey in CMA for coupling between antennas and the current study.

Reference	Scope	Main contribution	Measurements
[11]	Multimode MIMO (FF)	Evaluating radiation and mitigating coupling in a hexagonal antenna working in the frequency band from 3 to 6 GHz.	Yes
[12]	Wideband dipole structures (FF)	A novel design approach using CMA and equivalent circuit models for broadband planar antennas.	No
[13]	Patch antenna (FF)	Enhancing patch antenna bandwidth and gain by minimizing side lobe radiation via CMA coupling.	Yes
[14]	General two-antenna system (NF)	Refining the CMA procedure in the FF with modal NF distributions to optimize antenna prototypes and suppress undesired CMs.	Yes
[15]	U-Slot patch antenna (NF and FF)	Introducing a design approach through the creation of an equivalent circuit via CMA and CMT describing the impedance characteristics of a traditional U-slot patch.	Yes
[16]	SCMR and CSCMR systems (NF)	Conducting the NF modal distributions of the dominant CM.	No
[17]	Coupled split-ring resonators (NF)	Revealing the influence of the feed impedance and the aptness of rotational orientation of a pair of closely spaced SRR.	No
[18]	Out of band antenna mutual coupling (FF)	Optimizing inductive load positions to minimize out-of-band interference caused by antenna mutual coupling.	Yes
[19]	Wire and loop antennas (NF)	Determining optimal positions and values of loads for wire and loop antennas using CMA to suppress NF and out-of-band coupling.	No
[20]	WPT using loop antennas (NF)	A comparative study between three WPT systems using CMA.	No
This work	**WPT using loop antennas (NF and FF)**	**Providing an analysis procedure to investigate the coupling between circular loop antennas under various misalignment scenarios, and validating simulation outcomes through measurements**.	**Yes**

Therefore, researches have subsequently focused on the goal of increasing the energy acquisition for electric-driven devices over greater distances and increasing the tolerance to misalignment. Within this framework, numerous studies have been conducted to analyze and develop models for the coupling within Magnetically Coupled Resonant Wireless Power Transfer (MCR-WPT). The main objective consists of enhancing the PTE of WPT systems by comprehending the influence of critical parameters, such as antenna size, separation distance, and misalignment on the effectiveness of the system. For instance, proposed techniques include circuit-based analysis [21], and the application of mathematical equations in analytical modeling [22]. Yet, to verify their accuracy with the intended challenges of WPT systems, those coupling analysis methodologies attempts to adhere to experimental measurements. Thus, hybrid modeling, which consists of combining experimental measurement and coupling analysis, provides more precision regarding the efficiency and the effectiveness of the WPT system in real applications.

Characteristic Modes Analyses (CMA) [23], [24] have provided powerful insights into the radiating phenomena of antennas and succeeded to overcome the design challenges related to complicated structures. In particular, the theory has been widely used as a powerful tool in various research works to interpret and understand coupling and decoupling between antennas in both NF and FF regions, as delineated in Table 1. For instance, CMA of FF coupling were deployed to improve the design and the modeling of wideband planar antennas [12], and to enhance the gain of patch antennas [13]. In a recent communication, CMA has adopted and validated to analyze the NF coupling between general two-antennas systems [14], [15]. Indeed, by introducing the modal NF properties, the original procedure for the CMA in the FF can be modified to recognize the functional and nonfunctional modes through comprehensive usage of the modal admittance, and the distributions of the modal magnetic NF and the eigen currents. Other investigation [15] developed first principles mechanism to examine the U-slot patch antenna design methodology, where CMA and Coupled Mode Theory (CMT) were used to optimize the slot shape and the probe location by analyzing the coupling between the two resonators in the NF region. Subsequently, researchers notably utilized CMA to delve into modal characteristics of coupling within various WPT systems, including Strongly Coupled Magnetic Resonance (SCMR) [16], Split-Ring Resonators (SRR) units [17], and different MCR-WPT systems [20]. However, only simulations results executed through the electromagnetic simulators FEKO and CST Microwave Studio were interpreted in the previous studies, and very limited forms of misalignments were outlined.

This recent investigation has raised the interest in the analysis and measurement of megahertz (MHz) MCR-WPT systems. Given the swift advancements in power electronics over the past decades, particularly the increased switching frequencies of power semiconductor devices, MHz WPT systems has garnered attention [25]. In particular, with the two loops perfectly aligned and separated by a distance

of 3 cm (0.04λ), the system's resonant frequency (f_{res}) is equal to 416 MHz. The present work aims to utilize the concepts given by the CMA governed by the CMT to develop a more generalized investigation of MCR-WPT systems, which is simultaneously applicable to both the NF and FF coupling between loop antennas. Misalignment effect in several practical scenarios will be analyzed in terms of CMA. The most important distinctions between the previous works and the present paper relays on drawing analogies between the simulations and the measurements results of the fabricated prototypes. This study serves to expand upon existing knowledge by correlating the two and providing an illustrative application of the proposed methodology. Importantly, it acknowledges the adaptability of the system to be scaled for targeting precise frequencies tailored to specific WPT applications.

The remaining sections of this paper are organized in the following pattern. A thorough examination of coupling utilizing the Theory of Characteristic Modes (TCM) is reported in Section II, encompassing an introduction to both the mathematical and physical underpinnings of the theory. This includes as well a description of the coupling within the MCR-WPT system using CMA. In Section III, the different proposed misalignment scenarios under analysis are described and meaningful results are presented to clearly trail the modal interaction intrinsic to the coupling and the frequency shift. To demonstrate the measured WPT characteristics of the antenna, comparison between simulations and measurements of the PTE and the frequency shift governed by the CMT are addressed in Section IV. Finally, the validation of the proposed study with the measurements outcomes are reported in Section V.

II. INTRODUCTION TO CMA OF COUPLING

As indicated in Table 1, a variety of analytical methods and procedures based on Characteristic Modes (CMs) were developed to describe electromagnetic field distributions and the interaction between different antennas. From here, to analyze coupling by utilizing CMA, one single loop and a system comprising two identical loops (Tx as the transmitter loop and Rx as the receiver loop) will be analyzed using CM. For the sake of understanding of the CMA results, a brief introduction to the TCM, followed by an examination of its out-performance over existing techniques will be firstly conducted.

A. BRIEF MATHEMATICAL REVIEW OF THE THEORY OF CHARACTERISTIC MODES

The TCM is based on the decomposition of the surface current density $\vec{J}$ of an arbitrary shaped structure into a set of real orthogonal basis currents $\vec{J}_n$. This modal subdivision enables the subsequent analysis and the excitation of antennas through visual and suitable information of the radiation mechanisms, where the eigenvectors $\vec{J}_n$ and their associated eigenvalues λ_n of the n^{th} CM are calculated using the MoM complex generalized impedance matrix $[Z]$ of the structure, as follows [23], [24]:

$$[X](\vec{J}_n) = \lambda_n [R](\vec{J}_n) \tag{1}$$

where $[X]$ and $[R]$ stand for the imaginary and the real parts of $[Z]$, respectively. Furthermore, the surface current density $\vec{J}$ and the characteristic currents $\vec{J}_n$ are related through the Modal Weighting Coefficient (MWC) α_n, i.e:

$$\vec{J} = \sum_n \alpha_n \vec{J}_n = \sum_n \frac{V_n^i}{1 + \mathrm{j}\lambda_n} \vec{J}_n \tag{2}$$

where V_n^i describes the Modal Excitation Coefficient (MEC). Equation 2 includes as well the eigenvalues λ_n, which depend on the frequency, provide information about the resonance of the associated CM, and describe the distribution of the electromagnetic energy associated to the CMs of the structure. Indeed, the resonance of a given CM is defined when its λ_n=0. In addition, when λ_n is negative, the mode predominantly stores electric energy and it is considered capacitive. However, when it is positive, the mode predominantly stores magnetic energy and it is inductive. Typically, as the variation range of eigenvalues λ_n is from $-\infty$ to $+\infty$, they do not provide the best representation of CMs. Thus, various modal attributes were proposed for better physical interpretation of the eigenvalues [26], such as the Modal Significance (MS_n), the Characteristic Angle (CA_n), or the modal quality factor (Q_n). In this analysis, the characteristic angle (CA_n), defined by the following mathematical formulation, is going to be used to determine the resonant frequencies of the CMs contributing in the power transmission scenario:

$$CA_n = 180° - arctan(\lambda_n) \tag{3}$$

With correspondence to the resonance condition, a CM resonates when its CA_n is equal to 180°. Physically, this later presents the phase angle between the modal electric field $\vec{E}_n$ and its corresponding $\vec{J}_n$.

B. ADVANTAGES OF CMA OVER EXISTING TECHNIQUES FOR WPT ANALYSIS

Pioneering investigations have delved into analysing, optimising and evaluating WPT antenna systems using various approaches, such as Equivalent Circuit Analysis (ECA) [27], Modeling (AM) [28], Numerical Methods (NM) [29], and Experimental Testing [30]. These methods have been employed in various studies across the literature for broad coupling analysis in diverse applications. Providing distinct insights into coupling between antennas, CMA has demonstrated its capacity to assimilate existing techniques by providing a deeper understanding of the underlying physics as shown in Table 2. In the context of WPT, the decomposition of a complex system into its constituent modes by the means of CMA, where each CM represents a unique pattern of energy distribution has brought significant benefits in understanding the behavior and the influence of the different analyzed

TABLE 2. CMA integrating existing antenna WPT analysis techniques: a literature review.

Reference		ECA	AM	NM	Experimental testing	Modal features
Various Applications	[11]	✓	✓	✓	✓	Modal coupling and radiation.
	[12]	✓	✓	✓	×	Modal impedance model and CMT of resonant modes.
	[14]	×	✓	✓	✓	Modal NF and eigen-current distributions, modal self-admittance, and modal mutual admittance.
	[15]	✓	✓	✓	✓	Charge and current distributions, modal weighting coefficients, eigen-currents, Modal far-fields, CMT, and modal circuits.
WPT	[16]	×	✓	✓	×	Modal magnetic field and eigen-current distributions and Modal Angles,
	[17]	×	✓	✓	×	Excited resonant modes, modal significance, and eigencurrent distributions.
	This work	×	✓	✓	✓	**Resonant modes, modal angles, CMT, modal power patterns, and modal magnetic NF and eigen-current distributions.**

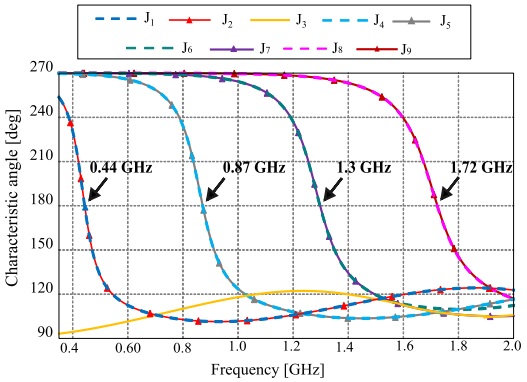

FIGURE 1. Characteristic Angle (CA_n) of the CM associated to the Tx loop antenna, within the frequency range from 0.35 to 2 GHz.

aspects on the coupling features between antennas for WPT applications.

In greater detail, by comparing the modal approach of the SCMR and CSCMR systems [16], CMA exposed the coupling between the Tx and the Rx antennas by conducting the dominant CMs and their properties near their resonances. Indeed, CMA was deployed to discern the modes providing robust inductive coupling and efficient PTEs, which are intricately linked to the capacitance values within the Tx and Rx resonators of both systems. Moreover, in [17], a detailed examination of the WPT given by coupled SRR units was conducted by exposing the CA_n and the current distributions of the resonant modes through the variation of two key parameters, which are the position and the impedance of the feeding ports of the split gaps of the rings. Notably, some CMs having particular resonant frequencies related to the analyzed scenarios were exhibiting better performances in terms of the PTE, which makes CMA a powerful tool for the design of SRR-based magneto-inductive WPT links by exciting some modes and mitigating others. Although these preceding studies had demonstrated notable efficacy, they solely interpreted simulation outcomes conducted via electromagnetic simulators like FEKO and CST Microwave Studio, with very limited forms of misalignment considerations. To serve as a comprehensive reference and to inspire future research on CMA, the present work compares empirical and experimental results across various misalignment scenarios between Tx and Rx loops antennas. Thus, it serves as a valuable reference for future researchers seeking to establish foundational knowledge about CMA for WPT, assessing its advantages, feasibility, and associated challenges in commercial and industrial applications.

C. CMA OF THE TX LOOP

This section will involve presenting the CMA of a Tx loop antenna, from 350 MHz to 2 GHz frequency band, to better comprehend the impact of coupling within the proposed conditions when a second loop is introduced.

In this investigation, the loops in both the Tx and Rx units have a diameter (D) of 23.18 cm ($\simeq 0.3\lambda$) and are constructed using a metal wire with a thickness (w) of 0.14 cm. Fig. 1 displays the CA_n associated to the first nine modes within the frequency range of 0.35 GHz to 2 GHz. The results reveal the presence of four sets of degenerated modes, where each comprising two resonating modes with identical resonance frequencies. Clearly, the first pair resonates at 0.44 GHz, the second pair at 0.87 GHz, the third pair at 1.3 GHz, and the fourth pair at 1.72 GHz. For the sake of clarity, the eigen currents and their associated magnetic NF distributions in XY-plane for the different CM of the Tx loop are presented in Fig. 2, where the degenerated modes have been arranged in a consolidated manner within a single row. The schemes of eigen currents presented along the wire structures in Fig. 2 with correspondence with the modal behavior in Fig. 1 show that the observed degenerated modes have the same current distribution with a 90° phase difference. Each increase in the

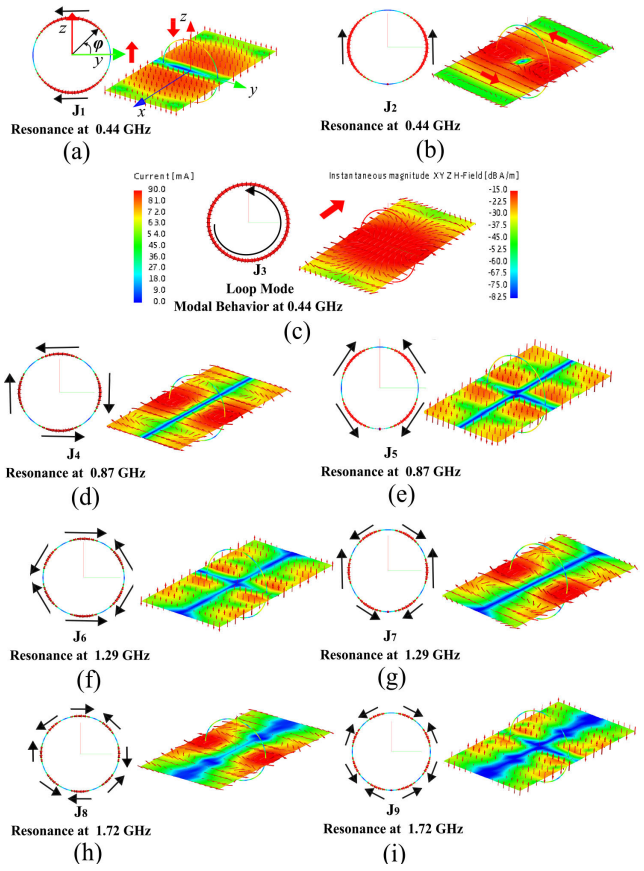

FIGURE 2. Eigen currents and their associated magnetic NF distributions in XY-plane for the different CM of the Tx loop: (a) J_1; (b) J_2; (c) J_3; (d) J_4; (e) J_5; (f) J_6; (g) J_7; (h) J_8; (i) J_9.

order of the mode set involves an escalation in the number of current nulls placed along the perimeter of the loop. For instance, J_1 exhibits two nulls distributed at $\phi = 0°$ and $\phi = 180°$, while J_8 comprises eight nulls positioned at $\phi = 30°$, 60°, 120°, 150°, 210°, 240°, 300°, and 330°. Fig. 2(c) illustrates the third mode J_3, characterized as a non-resonant mode, wherein the current distribution manifests a complete loop devoid of any nulls.

Additionally, from the magnetic NF distributions in the XY-plane perspective, it is evident that higher-mode orders correspond to weaker magnetic fields. Thus, the excitation of the lower order CMs (J_1, J_2, and J_3) is advantageous for achieving a strong and uniform magnetic field in proximity to the Tx loop. Exciting these CMs contributes enormously in bolstering coupling and optimizing the PTE.

D. CMA OF A MCR-WPT SYSTEM

In this subsection, a MCR-WPT system consisting in a Tx and a Rx loop will be analyzed using CMA.

In the CMA, the introduction of a second loop in the proximity of the Tx loop has decomposed the different $\vec{J}_n$ in two categories [31]. The first contains the CMs whose current distribution is the same at both coils and it is flowing

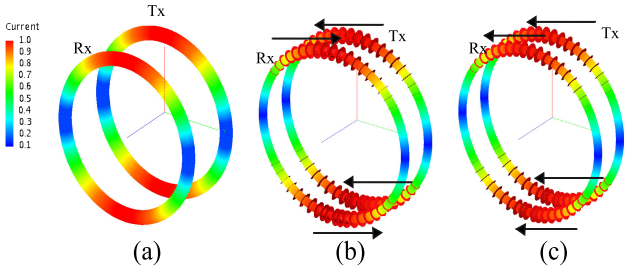

FIGURE 3. (a) The normalized current distribution of the MSC-WPT system near its resonance; (b) The associated Transmission Line Mode (TLM) configuration; (c) The associated Antenna Mode (AM) configuration.

in the same direction. They are called Antenna Modes (AM), and usually present a smooth variation in the CA_n near the resonance frequency. Conversely, when the currents on the two loops have the same intensity but flow in opposite directions, the modes are called Transmission Line Modes (TLM), and they typically exhibit a steep variation in the CA_n near the resonance. The CMA contributed in the recognition of different sets of CMs, and each one of them contains an AM with its TLM. Fig. 3 shows the configuration of a TLM through the current distribution presentation of two parallel loops.

This paper will explore later the variation of the coupling between two loops under different misalignment scenarios, based on a detailed physical description of the fields and the CMs. Thanks to the CMT, the energy exchange, the coupling coefficients, the frequency shift, and the influence of each AM on its associated TLM characteristics were processed at different separation distances using the following equation of the resonance frequencies of coupled CMs [15], [31], [32], [33]:

$$\omega = \frac{\omega_1 + \omega_2}{2} \pm \sqrt{\left(\frac{\omega_1 - \omega_2}{2}\right)^2 + |k_{1\longleftrightarrow 2}|^2} \tag{4}$$

where ω_1 and ω_2 are respectively the resonance frequencies of the AM and its associated TLM, respectively, and $k_{1\longleftrightarrow 2}$ is the coupling coefficient between these two CMs. Hence, a distinctive representation of the normalized coupling coefficient between the AM and its corresponding TLM, derived from (4), might be expressed as:

$$k_{1\longleftrightarrow 2} = k_{TLM\longleftrightarrow AM} = \frac{|\omega_{AM}^2 - \omega_{TLM}^2|}{\omega_{AM}^2 + \omega_{TLM}^2} \tag{5}$$

The forthcoming sections will methodically delve into the CMA of the proposed scenarios, aligning with the earlier outlined equations.

III. CMA FOR VARIOUS MISALIGNMENTS IN MCR-WPT SYSTEM

This section will explore the variation of the coupling between Tx and Rx loops under different misalignments scenarios shown in Fig. 4, and adhering to the order presented in Table 3. In the MCR-WPT system, the Tx loop is excited by a voltage source as shown in in Fig. 4(a), and the Rx loop

TABLE 3. Detailed description of the proposed misalignment scenarios under analysis.

Type of misalignment	Position of the Rx center to the source center	Azimuthal angle	Rotational angle of the Tx excitation	Rotational angle between the Rx center and the source center
(1) Lateral along the x-axis	$0.5\text{ cm} \leq \Delta x \leq 50\text{ cm}$	$\theta = 0°$	$\varphi = 0°$	$\Psi = 0°$
(2) Lateral along the y-axis	$\Delta x = 3$ cm $\lvert \Delta y \rvert \leq 20$ cm	$\theta = 0°$	$\varphi = 0°$	$\Psi = 0°$
(3) Azimuthal	$\Delta x_1 = 3$ cm $\Delta x_2 = 10$ cm	$-8° \leq \theta_1 \leq 8°$ $-40° \leq \theta_2 \leq 40°$	$\varphi = 0°$	$\Psi = 0°$
(4) Rotation of the excitation port	$\Delta x = 3$ cm	$\theta = 0°$	$0° \leq \varphi \leq 180°$	$\Psi = 0°$
(5) Rotation of the Rx	$R = 15$ cm	$\theta = 0°$	$\varphi = 0°$	$0° \leq \Psi \leq 360°$

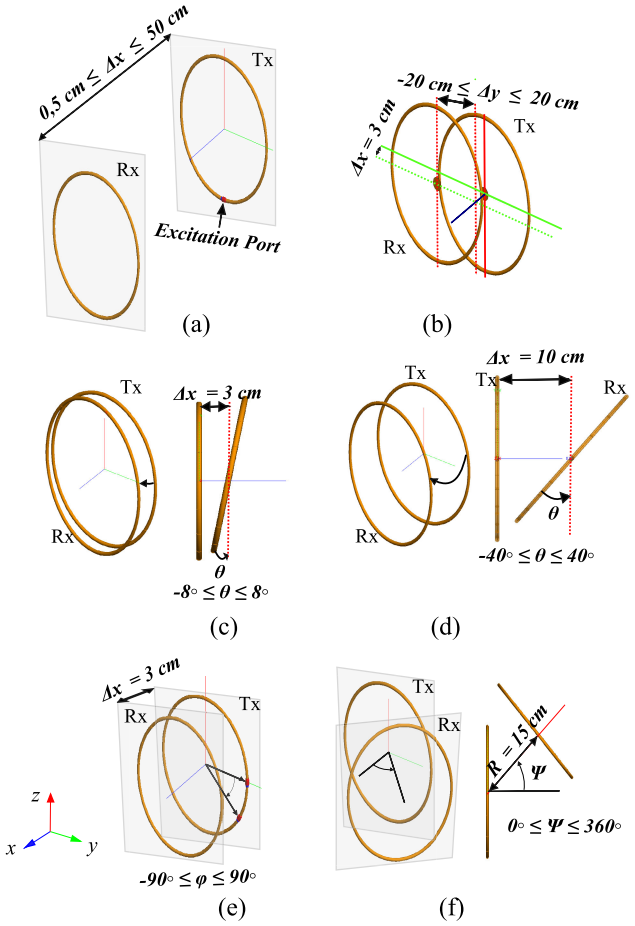

FIGURE 4. Depiction of the five distinct misalignment scenarios under analysis: (a) Lateral misalignment along the x-axis; (b) Lateral misalignment along the x-axis and y-axis; (c) Azimuthal misalignment at $\Delta x = 3$ cm; (d) Azimuthal misalignment at $\Delta x = 10$ cm (e) Rotational misalignment of the excitation port; (f) Rotational misalignment of the Rx.

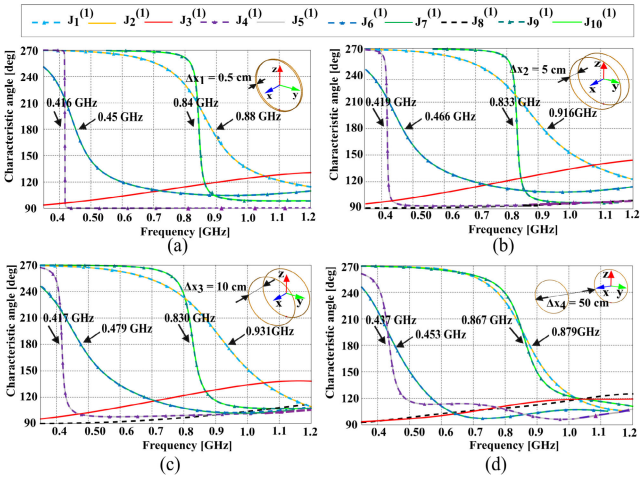

FIGURE 5. The impact of increasing the lateral misalignment along the x-axis on the CA_n of the antenna system at: (a) $\Delta x_1 = 0.5$ cm; (b) $\Delta x_2 = 5$ cm; (c) $\Delta x_3 = 10$ cm; (d) $\Delta x_4 = 50$ cm.

has a port at the same position, where the received power is measured. Utilizing FEKO, it is possible to control the power level at the source port of the Tx loop. Thus, a uniform input power of 330 mW is maintained for the proposed scenarios. The received power at the load port of the Rx loop is then measured, considering the contribution of the different CMs.

To simplify and accommodate the diverse eigen currents of the different configurations, their notation approach adopts the format $J_j^{(i)}$, wherein two discrete indices, labeled as j and i, are utilized. In this context, the sub-index j corresponds to the mode order linked to the respective misalignment scenario represented by the super-index i (see Table 3). For instance, $J_2^{(1)}$ represents the second CM of the lateral misalignment along the x-axis.

A. LATERAL MISALIGNEMENT ALONG THE X-AXIS

Starting by an examination of the initial scenario illustrated in Table 3 in conjunction with Fig. 4(a), the inter-antennas separation along the x-axis includes four discrete settings, spanning from 0.5 cm to 50 cm, which are approximately equal to 0.007λ and 0.7λ. Thus, the separation range extends from the NF to the FF zone, encompassing distances greater than $\lambda/2$.

To illustrate the diverse variations of CMs with regards to the increase of the lateral misalignment, the CA_n simulated with FEKO and associated to the described misalignment, sketched in Fig. 5 over a frequency range from 0.35 to 1.2 GHz, highlight the gradual changes. The figure illustrates

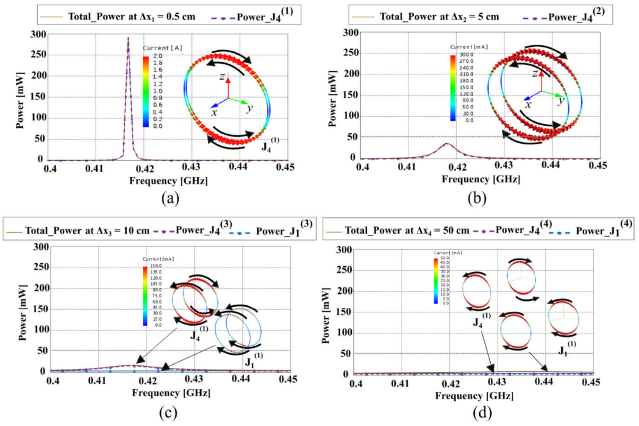

FIGURE 6. The impact of increasing the lateral misalignment along the x-axis on the total power of the system, the contribution of the dominant CMs and their current distributions near their resonances at: (a) $\Delta x_1 = 0.5$ cm; (b) $\Delta x_2 = 5$ cm; (c) $\Delta x_3 = 10$ cm; (d) $\Delta x_4 = 50$ cm.

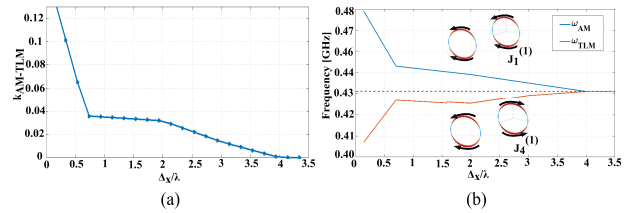

FIGURE 7. Modal intercoupling analysis when the lateral misalignment lies between $\Delta_x = 0.14\lambda$ and $\Delta_x = 3.5\lambda$: a) Normalized coupling coefficient between $J_1^{(1)}$ and $J_4^{(1)}$; b) The resonance frequency of $J_1^{(1)}$ and $J_4^{(1)}$.

the presence of two distinct groups of resonant modes, and two subsets of degenerated CMs within each group. Each subset is characterized by the coexistence of two AMs and two TLMs, each with varying resonant frequencies. For instance, in Fig. 5(a), there exists a first group of modes composed by a degenerated pair of TLMs ($J_4^{(1)}$ and $J_5^{(1)}$) and a pair of AMs ($J_1^{(1)}$ AND $J_2^{(1)}$). Note that the resonance frequency of each set of degenerated CM is also shown in the figure.

With the progressive increment in the separation distance between the loops, as illustrated in Fig. 5(b) and Fig. 5(c), a discernible frequency shift is observed. Following this approach, when the antennas are positioned at a considerable distance from each other, as depicted in Fig. 5(d), the modes within each group converge to nearly identical resonant frequencies.

To identify the modes that have the greatest impact on the system power, Fig. 6 presents the total power received by the system alongside the corresponding contributions of the dominant CMs at the different distances. As observed, at short distance, the power of the MCR-WPT system is governed by the TLM $J_4^{(1)}$. However, the contribution of the AM $J_1^{(1)}$ is involved when the separation between the two loops is increased. As shown in Fig. 6(d), this fact induces a significant diminution in the system power. Significantly, the

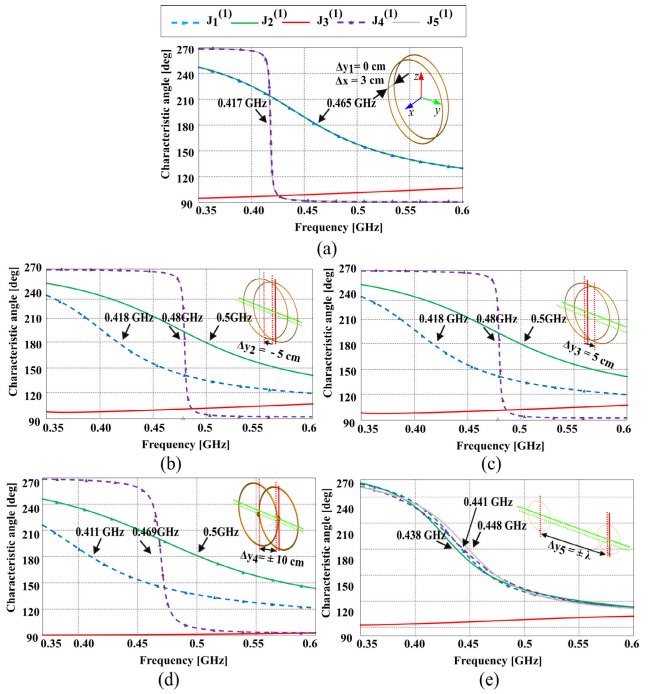

FIGURE 8. The impact of increasing the lateral misalignment along the y-axis at $\Delta x = 3$ cm on the CA_n of the antenna system at: (a) $\Delta y_1 = 0$ cm; (b) $\Delta y_2 = +5$ cm. (c) $\Delta y_3 = -5$ cm; (d) $\Delta y_4 = \pm 10$ cm; (e) $\Delta y_4 = 63$ cm ($\pm\ \lambda$).

present analysis aligns well with reference [42], corroborating the assertion that the TLM $J_4^{(1)}$ predominantly contributes to the overall power of the system at close ranges.

To compute the normalized intercoupling between $J_1^{(1)}$ and $J_4^{(1)}$ using Eq. 5, Fig. 7(a) shows the variation of $k_{J_1^{(1)} \longleftrightarrow J_4^{(1)}}$ due to the incremental lateral misalignment, and Fig. 7(b) illustrates the resonance frequencies of the modes. Those results show that the coupling between the two antennas are contingent upon the intercoupling between the dominant TLM $J_4^{(1)}$, and its associated AM $J_1^{(1)}$. As the separation distances increase, the frequency shift of the two modes becomes increasingly prominent, and they converge precisely to the same resonance frequency (f_{res}), which is presented by the dotted line in Fig. 7(b). This later corresponds to the f_{res} of J_1, which was previously identified as the dominant mode of the single loop antenna. Indeed, the behavior of each of loop becomes entirely independent of the other.

B. LATERAL MISALIGNEMENT ALONG THE Y-AXIS

The second scenario described in Table 3 and illustrated in Fig. 4(b) involves situating the Rx unit at a fixed position on the x-axis, precisely 3 cm (0.04λ) away from the Tx, and modify the overlap along the y-axis (Δy). This particular separation distance in the x-axis is selected with respect to practical considerations of the Qi standard and the WPT applied for wearable and implementable devices.

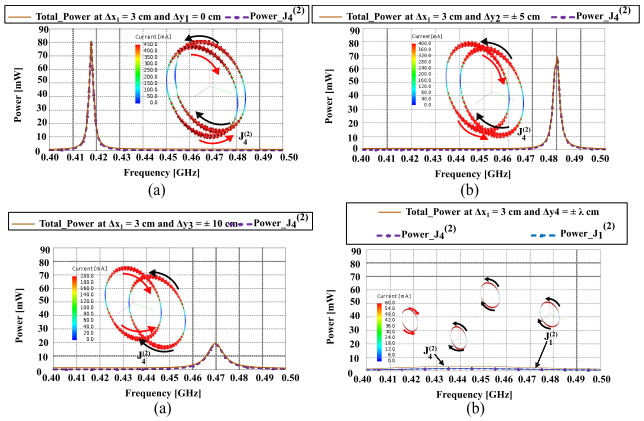

FIGURE 9. The impact of increasing the lateral misalignment along the y-axis on the total power of the system, the contribution of the dominant CMs and their current distributions near their resonances at: (a) $\Delta y_1 = 0$ cm; (b) $\Delta y_2 = \pm 5$ cm; (c) $\Delta y_3 = \pm 10$ cm; (d) $\Delta y_4 = 63$ cm ($\pm\ \lambda$).

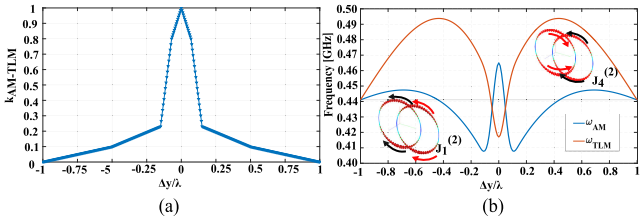

FIGURE 10. Modal intercoupling analysis when the lateral misalignment: (a) Normalized coupling coefficient between $J_1^{(2)}$ and $J_4^{(2)}$ for Δy between - 2λ and 2λ. b) The resonant frequency of $J_1^{(2)}$ and $J_4^{(2)}$ for Δy ranging from - λ and λ.

The CMA is shown in Fig. 8 and Fig. 9, where the frequency range is constrained to depict variations spanning from 0.35 GHz to 0.6 GHz, given that the lower-order CMs have demonstrated greater significance and efficacy in elucidating the coupling. The initial position, shown in Fig. 8(a), features the two loops perfectly aligned and their corresponding CA$_n$ present two sets of degenerated modes centered at two different frequencies. Then, the Rx loop is moved along the y-axis undergoing symmetrical displacements, ranging from -68 cm to 68 cm, which corresponds to $\pm\lambda$. Symmetric spatial configurations exhibit identical behavior, as shown in Fig. 8(b) and Fig. 8(c), which describe the CA$_n$ of the Rx antenna located at 5 cm and -5 cm respectively. Moreover, as shown in Fig. 9, TLM $J_4^{(2)}$ emerges as the dominant mode proximate to the resonance of the system in both configurations. Thus, the broader overlap distances, illustrated in Fig. 8(d) and Fig. 8(e), correspond to symmetric positions of Δy, which are $\pm$ 10 cm ($\pm 0.14\lambda$) and $\pm\lambda$.

By comparing Fig. 8(a) and Fig. 8(b), we observe that a slight incremental displacement of 5 cm (0.07λ) along the y-axis precipitates the dispersion of the CMs and a pronounced alteration in their resonance frequency becomes evident. By drawing analogies with the power simulations depicted in Fig. 9(a) and Fig. 9(b), it is evident that even a minor displacement significantly drains the power of the system. Furthermore, the frequency shift in the resonance of the system corresponds to the frequency alteration in the TLM, given the similarity between the peaks of both the overall system power and the dominant CMs. In extended separations and in the absence of coupling, as shown in Fig. 8(e), the TLMs and the AMs are converging perfectly to the same resonance. Indeed, the manifestation of the AM $J_1^{(2)}$, depicted in Fig. 9(c), present the absence of coupling between the Tx and Rx units.

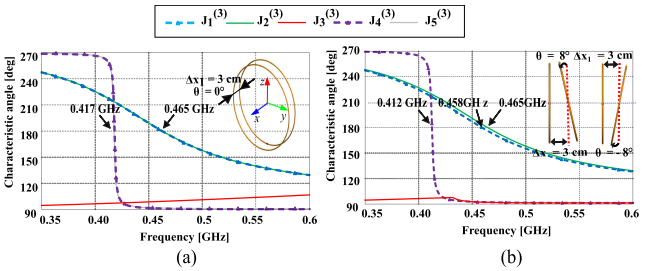

FIGURE 11. The impact of the azimuthal misalignment at $\Delta x_1 = 3$ cm on the CA$_n$ of the antenna system at: (a) $\theta = 0$ °; (b) $\theta = \pm 8$ °.

Fig. 10 depicts the coupling of the prevailing TLM and its corresponding AM. To compute $k_{J_1^{(2)} \longleftrightarrow J_4^{(2)}}$, the central configuration shown in Fig. 9(a), featuring neglected displacement on the y-axis, is identified as the configuration yielding the highest power, and it is delineated as the state wherein the system attains its optimal coupling coefficient. The coupling coefficient for alternate positions will be derived through referring to this configuration and it is shown in Fig. 10. As observed, an increase in overlapping induces a notable rise in the coupling existing between the AM $J_1^{(2)}$ and its corresponding TLM $J_4^{(2)}$. By comparing the results shown in Fig. 7(a) and Fig. 10(a), it can be seen the heightened sensitivity of coupling along y-axis overlap when compared to the misalignment coupling along x-axis. This observation aligns with a fundamental principle of WPT, advocating the parallel arrangement of Tx and Rx antennas.

C. AZIMUTHAL MISALIGNMENT

Azimuthal misalignment, defined by an angle θ, between two loop antennas refers to the angular deviation between their respective azimuth angles, as shown in Fig. 4(c) and Fig. 4(d). In practical scenarios, its occurrence arises from a non-parallel positioning of the Rx loop in relation to the Tx loop.

In this study, azimuthal misalignment is investigated under two distinct positional configurations, as the proximity of the two loops constrains the range of angular orientations. Initially, the Rx is situated with a displacement of 3 cm along the x-axis to the Tx, exhibiting two symmetrical azimuthal deviations, which are equal to $-8°$ to $+8°$. Later, the lateral misalignment between the two antennas expands to 10 cm (0.14λ), enabling the attainment of various azimuthal deflections that range from $-40°$ to $+40°$. The CMA on these two scenarios are conducted in the same section

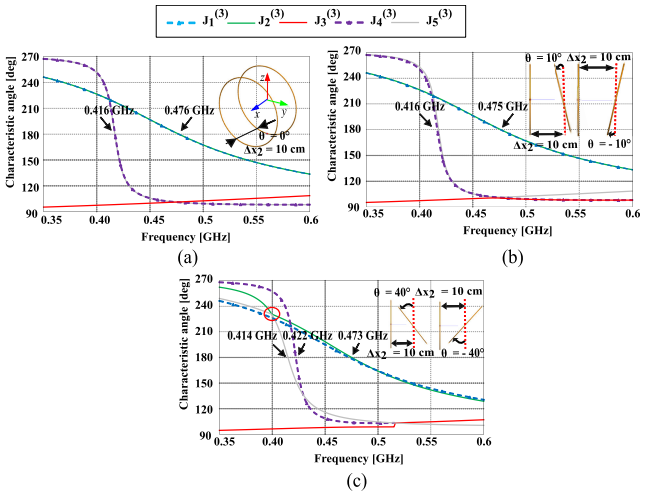

FIGURE 12. The impact of the azimuthal misalignment at $\Delta x_2 = 10$ cm on the CA_n of the antenna system at: (a) $\theta = 0°$. (b) $\theta = \pm 10°$. (c) $\theta = \pm 40°$.

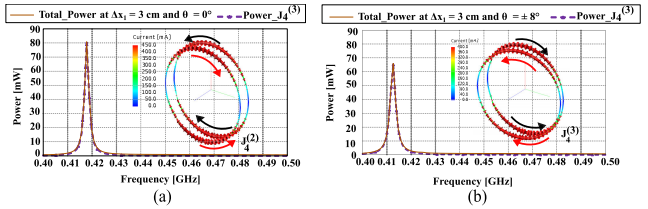

FIGURE 13. The impact of the azimuthal misalignment at $\Delta x_1 = 3$ cm on the total power of the system, the contribution of the dominant CM and its current distribution near its resonance at: (a) $\theta = 0°$. (b) $\theta = \pm 8°$.

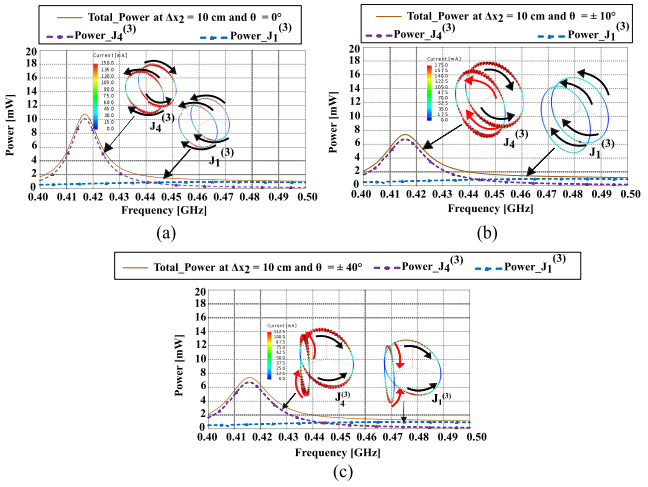

FIGURE 14. The impact of the azimuthal misalignment at $\Delta x_2 = 10$ cm on the total power of the system, the contribution of the dominant CMs and their current distributions near its resonances at: (a) $\theta = 0°$; (b) $\theta = \pm 10°$; (c) $\theta = \pm 40°$.

simultaneously to facilitate the observation of the angular deviations and lateral misalignment impact on the coupling behavior.

In Fig. 11(b) and Fig. 12(b), it becomes evident that a slight azimuthal misalignment of the Rx loop (θ=±8° and θ=±10°, respectively) has negligible impact on the modal

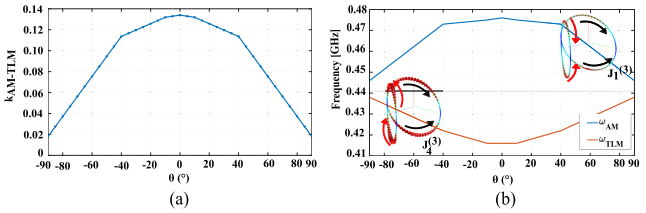

FIGURE 15. Modal intercoupling analysis when azimuthal misalignment at $\Delta x_2 = 10$ cm for θ between −90° and +90°: (a) Normalized coupling between $J_1^{(3)}$ and $J_4^{(3)}$; (b) The resonance frequency of $J_1^{(3)}$ and $J_4^{(3)}$.

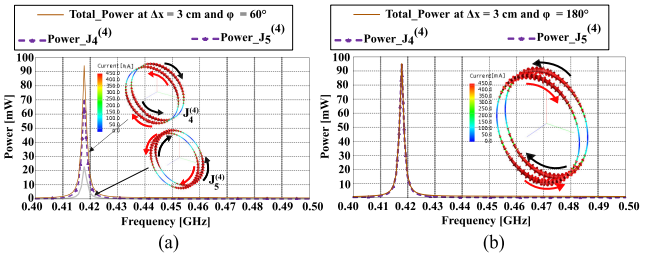

FIGURE 16. The impact of the rotational misalignment of the excitation port at $\Delta x_1 = 3$ cm on the total power of the system, the contribution of the dominant CMs and their current distributions near its resonances at (c) $\phi = 60°$; (d) $\phi = 180°$.

behavior by comparing to the CA_n of the initial position shown in Fig. 11(a) and Fig. 12(a). However, in Fig. 12(c), when the Rx loop is positioned at a greater distance with an azimuthal deviation of ±40°, the CA_n become disperse, and the effect of misalignment becomes more discernible. This behavior is similarly observed in the results shown in Fig. 13 and Fig. 14, wherein a slight azimuthal misalignment results in a relative slight reduction in the total power. Notably, the TLM $J_4^{(3)}$ consistently maintains its prominence and predominantly contributes to the overall power of the system.

In summary of all the interactions presented within the azimuthal misalignment, and considering the minimal influence observed at close distances, Fig. 15 depicts clearly the resonance frequency shift and modal coupling characteristics of both TLM $J_4^{(3)}$ and AM $J_1^{(3)}$, when the Rx loop is positioned at Δx_2 and the deviation of the positioning of the Rx coil encompasses an extended spectrum of angles. The analysis culminates in a configuration where the two coils achieve a state of complete perpendicular misalignment. As observed, azimuthal misalignment has a comparatively lesser impact than lateral misalignments.

D. ROTATIONAL MISALIGNMENT OF THE EXCITATION PORT PLACED ON THE TX LOOP

As described in Table 3 and Fig. 4(e), this misalignment scenario involves the precise parallel placement of the two coils with a separation of 3 cm (0.04λ). However, the positioning of the source excitation on the Tx loop undergoes different rotations. In particular, this scenario corresponds to a phenomenon wherein the device is situated haphazardly upon the wireless charger, resulting in the perfect parallel

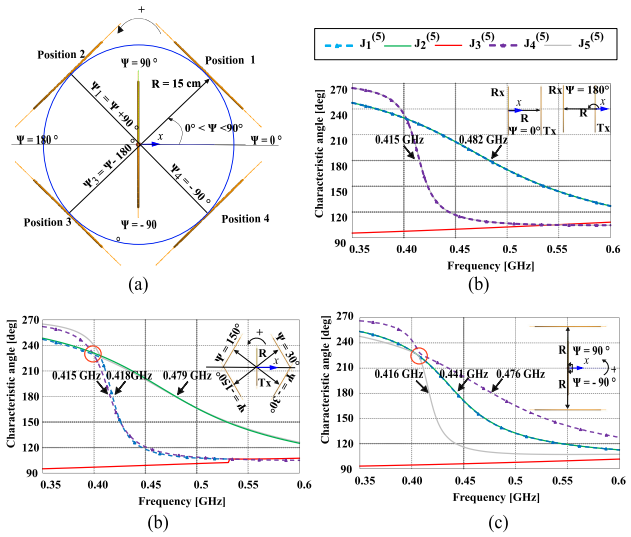

FIGURE 17. (a) Detailed description of the rotational misalignment of the Rx loop around the Tx loop with a radius R=15 cm, where the symmetrical positions 1, 2, 3 and 4 present the same CMA; (b) The impact of the CA_n of the antenna system at $\psi = 0°$ and 180°; (c) The impact of the CA_n of the antenna system at $\psi = \pm 30°, \pm 150°$; (d) The impact of the CA_n of the antenna system at $\psi = \pm 90°$.

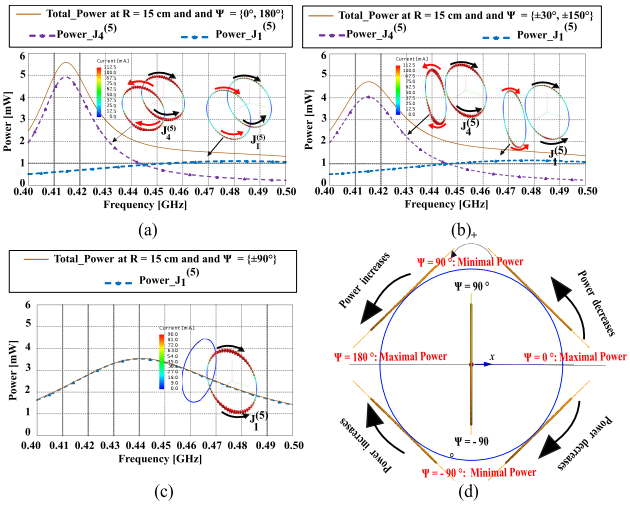

FIGURE 18. The impact of the rotational misalignment of the Rx on the total power of the system, the contribution of the dominant CMs and their current distributions near their resonances at: (a) $\psi = 0°$ and 180°; (b) $\psi = \pm 30°, \pm 150°$; (c) $\psi = \pm 90°$; (d) The variation of the total power.

alignment of the two coils. Nonetheless, the excitation port located at Tx and the load port positioned at Rx are not parallel, as described in Fig. 4(e).

As CM are independent of the excitation, it is obvious that rotations of the excitation port will not impact the modal behavior of the system, so CA_n will be those depicted already in Fig. 8(a). Furthermore, rotational misalignment of the Tx port will have little impact on the total power of the system, as shown in Fig. 16, where the received power exhibited consistently the values between 90 and 100 mW. This is due to the rotational symmetry of the current distribution of the CM of the loop. Notably, the TLM $J_4^{(4)}$ and its degenerated mode $J_5^{(4)}$ held a predominant contribution to the total system power. The contribution of these two modes depend on the rotation of the excitation port, and there exists no discernible presence of the AM within the power. This observation rationalizes the lack of decoupling between the two coils when contrasted with the preceding scenarios.

E. ROTATIONAL MISALIGNMENT OF THE RX COIL

This final scenario (described in Table 3 and illustrated in Fig. 4(f)) elucidates the CMA of the coupling within a WPT system, where the Rx coil executes rotational motion at specific distance around the Tx coil. This entails a stationary position for the Tx, while the Rx engages in circular rotation with a constant radius, thereby delineating a circular trajectory, as shown in Fig. 4(f). To enable this rotational movement, the radius of the circle R is set to 15 cm (0.21 λ), which leads to a substantial power loss. Therefore, an assessment of various positions of the Rx coil will be conducted relative to the initial configuration, where both the Tx and Rx antennas are perfectly aligned in parallel, as described in Fig. 17. During the course of these analyses, it was observed that the CMA and power radiation exhibit three distinct variations with respect to the rotation angle, as shown in Fig. 17 and Fig. 18. As observed in Fig. 18, the system attains its peak power levels during the initial and the final positions, denoted by ψ equal to 0° and 180°. As the rotation angle ψ increases within the range of 0° to ± 90°, the power of the system and the current intensity of the dominant mode $J_4^{(5)}$ decrease enormously by reaching a null value.

In this particular scenario, employing the resonance frequency equation for coupled CMs is challenging due to the overlapping frequencies of the relevant CMs, specifically $J_4^{(5)}$ and $J_1^{(5)}$, with other CMs. Consequently, the application of the suggested methodology for processing CMs necessitates identifying the specific resonance frequencies of $J_4^{(5)}$ and $J_1^{(5)}$. Fig. 17(c) and Fig. 17(d) depict the general tracking issue [34], emphasizing the intersection of CAs with red circles and a shift in the order of resonating CMs. Nevertheless, as explained, CMA offers a comprehensive interpretation of power variation as depicted in Fig. 18.

F. MAIN OBSERVATIONS: CMA OUTCOMES

The central aim of incorporating CMT into CMA in this study is to emphasize the substantial relationship between modal inter-coupling patterns, power fluctuations, and system efficiency across various misalignment scenarios, which will take place in the coming section. While previous research has explored this correlation in the context of WPT, it has been confined to limited misalignment scenarios and lacked experimental validations [20], [31]. This study introduces a broader range of scenarios to thoroughly test and assess the proposed technique.

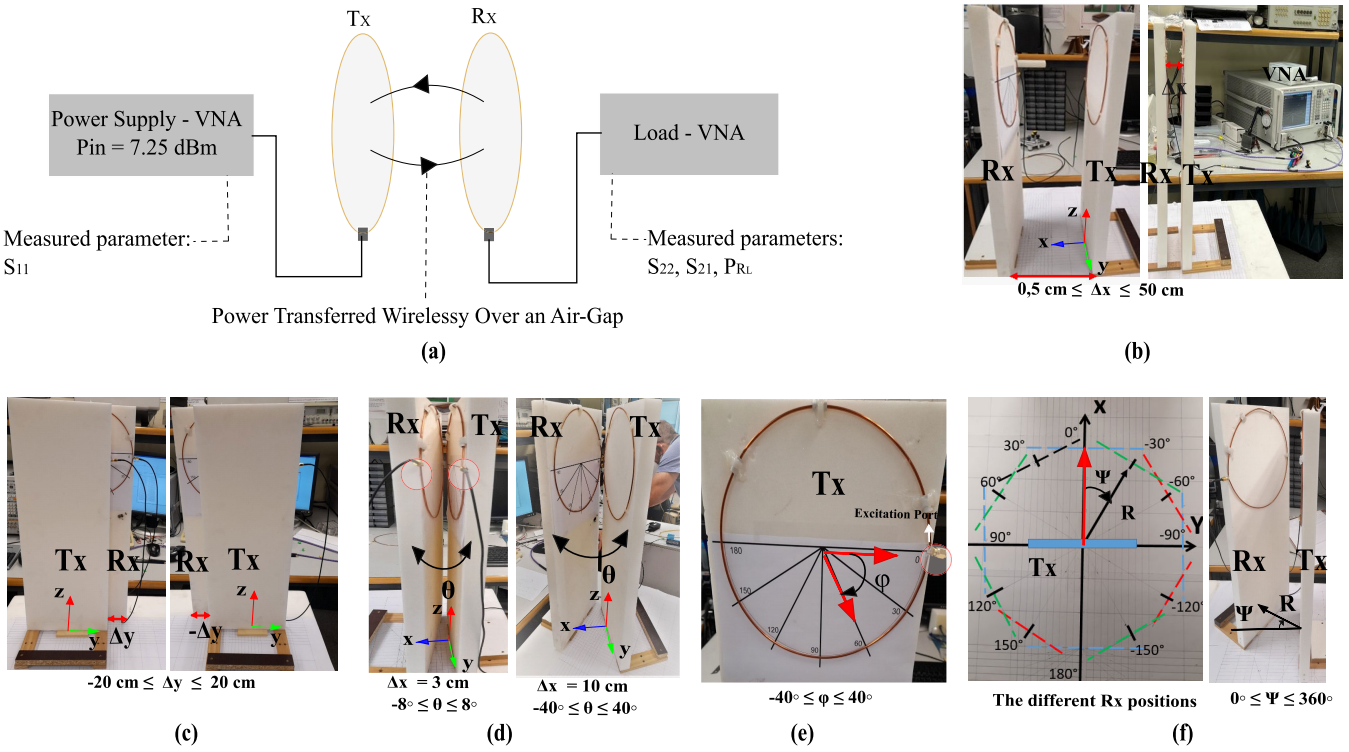

FIGURE 19. The measurements set-up of the different misalignements scenarios and their block diagram: (a) Block diagram of the Tx and Rx loops along with relevant components, (b) Lateral misalignment along the x-axis; (c) Lateral misalignment along y-axis at $\Delta x = 3$ cm; (d) Azimuthal misalignment at the two positions: $\Delta x = 3$ and $\Delta x = 10$ cm; (e) Rotational misalignment of the excitation port; (f) Rotational misalignment of the Rx.

In this section, CMA involved utilizing CA_n to identify resonant modes and their corresponding frequencies. Furthermore, the modal distribution of power was depicted to uncover the mode primarily influencing the power of the Rx coil, which is termed as the dominant mode. The eigen-currents distribution indicates that the latter is a TLM with horizontal nulls. Based on CMT, the modal inter-modal coupling was computed using the resonant frequencies of the TLM mode and its corresponding AM. The various modal features employed to assess the misalignment scenarios yielded consistent results. In particular, as the modal inter-coupling decreases, signifying precise frequency alignment between the dominant mode and its associated antenna mode, the system losses its efficiency, since the power level at the Rx coil diminishes entirely.

Moreover, the efficacy of this methodology depends on the proposed misalignment. For instance, in scenarios involving lateral and azimuthal misalignments, the modal resonant frequencies are clearly discernible. However, CMA of rotational misalignment of the Rx display tracking behavior, potentially complicating the precise observation of their resonant frequencies and rendering the utilization of CMT impracticable.

IV. MEASUREMENTS

The validation of the proposed analysis and simulations for the WPT system is achieved through measuring the S-parameters and evaluating the power received at the Rx coil with regards to the transmitted power set by the Network Analyzer (VNA) to the Tx coil, in the frequency margin from 0.3 to 0.6 GHz. Both Tx and Rx loop antennas were prototyped using copper, consisting of a diameter (D) of 23.18 cm ($\simeq 0.3\lambda$) and a wire with a thickness (w) of 0.14 cm. The measurement set-up of each scenario are shown in Fig. 19.

Table 4 provides a summary of the results, showcasing both the computed and measured power of the system across various configurations. In this table, $\text{PTE}_{\text{measured}^1}$ and $\text{PTE}_{\text{measured}^2}$ have been calculated using equations 6 and 7. Regarding $\text{PTE}_{\text{calculated}}$, the same expression used in Eq. 7, is used, but employing the S-parameters calculated by FEKO in this case [31], [35]:

$$\text{PTE}_{\text{measured}^1} = \frac{P_{R_L}}{P_{in}} = \frac{|I_2|^2 R_L}{|I_1|^2 R_{in}} \tag{6}$$

$$\text{PTE}_{\text{measured}^2} = \frac{|S_{21}|^2}{(1-|S_{11}|^2)(1-|S_{22}|^2)} \approx |S_{21}| \tag{7}$$

where P_{R_L} is the power dissipated in the load R_L of the Rx coil, P_{in} is the accepted power in the Tx antenna, R_{in} is the input resistance, and the currents in Tx and Rx antennas are I_1 and I_2 in Eq. 6, respectively.

In particular, the input power P_{in} is adjusted using the VNA, and it is set to 7.25 dBm. Similarly, the change in power at the Rx coil was directly measured using this later,

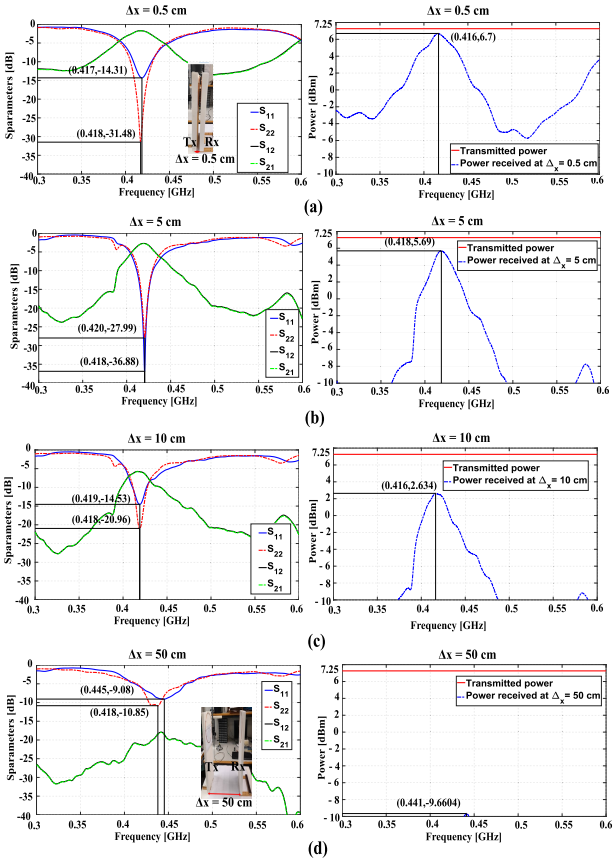

FIGURE 20. Measurements of the S-parameters (S_{11}, S_{22}, S_{21}, and S_{12}), and the PTE evaluation of the lateral misalignment configurations along the x-axis: (a) $\Delta x_1 = 0.5$ cm; (b) $\Delta x_2 = 5$ cm; (c) $\Delta x_3 = 10$ cm; (d) $\Delta x_4 = 50$ cm.

as shown in the block diagram presented in Fig. 19(a). The key parameters outlined in the preceding equations are obtained through measurements conducted using the VNA. This process enables the establishment of the various comparisons and facilitates drawing analogies with the CMA. Indeed, this study not only provides a comparison between theoretical and measured PTEs but also delves into a comprehensive exploration of the system's behavior from various perspectives. It highlights the two distinct forms of measured PTE, which adds depth to the investigation. Furthermore, the Table 4 displays the dominant CMs of the different scenarios along with their corresponding resonance frequencies. These frequencies are intended for comparison with the measured resonance frequency of the system, which corresponds to the peaks in the received power of the Rx coil.

The main goal of this section is to examine the correlation between CMA and the performance of the WPT system near its resonance. Consequently, by applying the techniques and methodologies outlined in the existing literature presented earlier in this study, it becomes feasible to better understand the coupling between two coils through CMA in order to enhance the PTE related to misalignment problems of WPT systems using coil antennas.

A. MEASUREMENT OF THE LATERAL MISALIGNMENT ALONG THE X-AXIS

To delve into further details, the initial measurement shown in Fig. 19(b), focusing on lateral misalignment along the x-axis, encompasses four distinct positions from the NF to the FF, ranging from 0.5 cm ($<\lambda/2$) to 50 cm ($>\lambda/2$).

When the separation distance is at its minimum, as shown in Fig. 20(a), the outcomes related to this misalignment in Table 4 indicate that the PTE reaches 88.67%, which corresponds to the highest value. In Fig. 20 (b) and Fig. 20(c), gradually increasing the separation between the Rx and Tx coils leads to a substantial reduction in coupling effectiveness. The system loses completely its efficiency in the final configuration shown in Fig. 20(d). Clearly, these findings are in complete accordance with the CMA across the different separation distances presented in Section B.2, especially that the f_{res} of the dominant mode, $J_4^{(1)}$, aligns with the system's measured f_{res}. Furthermore, the measured and the calculated PTEs follow the same variation pattern as the peaks of the analyzed CM power. Yet, it is worth noting that $\text{PTE}_{\text{measured}^1}$ that takes into consideration the levels of transmitted and received powers aligns more closely with the theoretical value when compared to $\text{PTE}_{\text{measured}^2}$.

B. MEASUREMENT OF THE LATERAL MISALIGNMENT ALONG THE Y-AXIS

In the second scenario depicted in Fig. 19(c), where a constant lateral misalignment of 3 cm is maintained along the x-axis, the measurements encompass a total of seven distinct positions of lateral misalignment along the y-axis. These positions include three pairs of symmetrical positions extending from -20 cm to +20 cm, along with the central position. As expected, there is a symmetry of the coupling behavior around the central position, when Δy equals zero.

Therefore, Fig. 21 illustrates lateral misalignments occurring along the positive y coordinates. However, while there is a strong correspondence between the analytical and experimental results for the initial and final positions in terms of the f_{res}, the intermediate positions, where Δy is equal to ± 5 and ± 10 cm, exhibit theoretically larger ranges of f_{res} in comparison to the measurements. For instance, by examining the f_{res} of the simulated system at the position ± 10 cm, shown in Fig. 9(a), which aligns with the resonance of the dominant CM $J_4^{(2)}$, it becomes apparent that it is roughly equal to 0.47 GHz. Yet, the variation of the measured f_{res} is shifted to lower frequency and it is equal to 0.403 as shown in Fig. 21(c).

Likewise, as observed in the previous misalignment analysis, the PTE measured using the ratio of Rx power to Tx power($\text{PTE}_{\text{measured}^1}$) tends to align more closely with the theoretical value, and it is worth highlighting that the theoretical values exceed the measured values at the largest range.

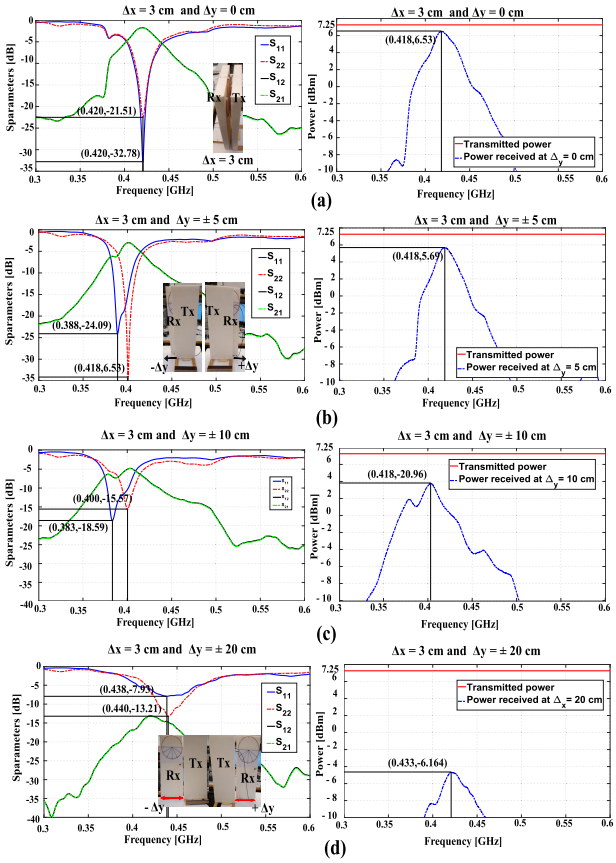

FIGURE 21. Measurements of the S-parameters (S_{11}, S_{22}, S_{21}, and S_{12}), and the PTE evaluation of the lateral misalignment configurations along the y-axis: (a) $\Delta_{y1} = 0.5$ cm; (b) $\Delta_{y2} = \pm 5$ cm; (c) $\Delta_{y3} = \pm 10$cm; (d) $\Delta_{y4} = \pm 50$ cm.

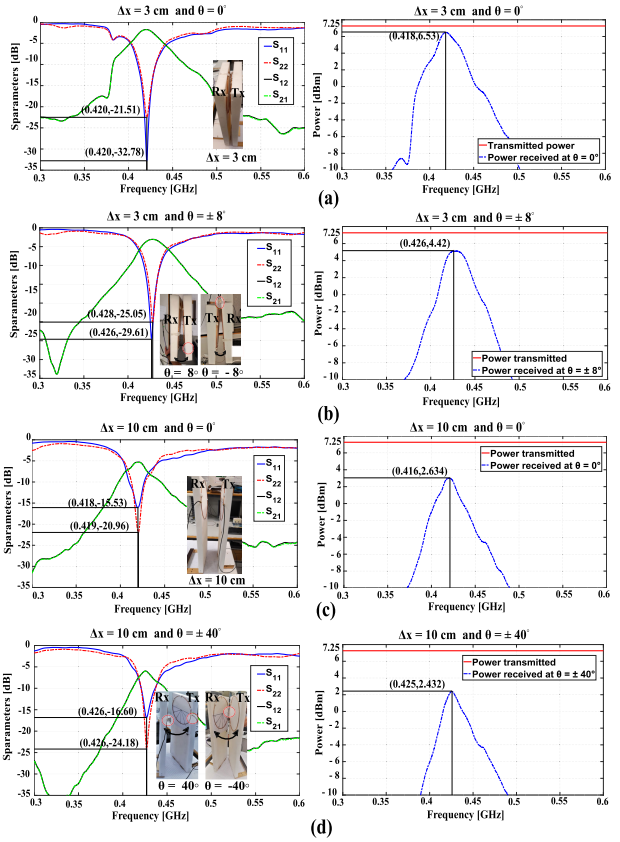

FIGURE 22. Measurements of the S-parameters (S_{11}, S_{22}, S_{21}, and S_{12}), and the PTE evaluation of the azimuthal misalignment configurations along: (a) $\Delta_x = 3$ cm and $\theta = 0°$. (b) $\Delta_x = 3$ cm and $\theta = \pm 8°$. (c) $\Delta_x = 10$ cm and $\theta = 0°$; (d) $\Delta_x = 10$ cm and $\theta = \pm 40°$.

C. MEASUREMENT OF THE AZIMUTHAL MISALIGNMENT

Regarding azimuthal misalignment shown in Fig. 19(d), as previously explained, the influence of angular rotations of the Rx coil along the z-axis on the system's performance was assessed at two distinct distances along the x-axis, since the angular rotations are restricted at short distances. As illustrated in in Fig. 22, at a short separation distance of 3 cm, two distinct measurement configurations were established, corresponding to θ values of $-8°$ and $+8$. In contrast, when considering a greater separation distance of 10 cm, the conducted experiments encompassed larger symmetrical azimuthal variations reaching $-40°$ and $+40°$.

The values presented in Table 4 reveals that the azimuthal misalignments introduce a slight reduction in the values of the three PTEs, when compared to the initial configuration at θ equal to 0°. Besides, it is noteworthy that the PTE computed using the ratio of received and transmitted powers exhibits a stronger resemblance to the PTE calculated through FEKO. In instances of close-range scenario, the azimuthal misalignment leads to a 4% decrease in PTE, whereas, with an increase in the separation distance, the measured PTE experiences an almost 2% reduction under the most substantial misalignment condition with a θ value of $+40°$. Consequently, it is apparent that azimuthal misalignment has a relatively modest impact on the overall PTE of the system when contrasted with previous scenarios.

In the context of CMA, the measurement findings align closely with the analysis presented in the preceding section. Specifically, the modal coupling, which refers to the interaction between the TLM and its associated AM, exhibited no reduction and remained consistently at the same level for identical values of the angular misalignments.

D. MEASUREMENT OF THE ROTATIONAL MISALIGNMENT OF THE EXCITATION PORT PLACED ON THE TX LOOP

Fig. 23 displays measurements of the rotational misalignment of the excitation port of the Tx coil, which are represented Fig. 19(e). The range for φ spans from 0° to 180°, with a 30° increment between each successive experiment. In Table 4, to emphasize the key observations, the initial configuration, where the excitation port and receiving port are perfectly aligned, is compared with two distinct cases. The first case involves a minor deviation of 30° in the excitation port, while the second case examines the most significant deviation, equivalent to 180°. These measurements allow us to reveal essential insights that align with CMA. In the various configurations, the CAs consistently remained unchanged and the eigenvalues exhibited resonance at the same frequencies.

TABLE 4. Comparison between CMA and measurements of the WPT system characteristics under the various misalignment scenarios.

Type of misalignment			Dominant CM	Computed f_{res} of the dominant CM (GHz)	Measured f_{res} of the system (GHz)	$PTE_{calculated}$	$PTE_{measured^1}$	$PTE_{measured^2}$
Lateral along the x-axis	$\Delta x = 0.5$ cm		$J_4^{(1)}$	0.416	0.416	87.55%	88.67%	76.25%
	$\Delta x = 5$ cm		$J_4^{(1)}$	0.419	0.418	73.99%	69.81%	53.00%
	$\Delta x = 10$ cm		$J_4^{(1)}$	0.417	0.416	53.47%	33.96%	26.02%
	$\Delta x = 50$ cm		$J_4^{(1)}$	0.437	0.441	0.19%	0.018%	0.031%
Lateral along the y-axis at Δx=3 cm	$\Delta y = 0$ cm		$J_4^{(2)}$	0.417	0.418	82.09%	84.90%	66.56%
	$\Delta y = \pm 5$ cm		$J_4^{(2)}$	0.460	0.401	83.23%	67.92%	49.45%
	$\Delta y = \pm 10$ cm		$J_4^{(2)}$	0.469	0.403	66.77%	45.28%	33.34%
	$\Delta y = \pm 20$ cm		$J_1^{(2)}$	0.441	0.433	16.15%	5.89%	5.01%
Azimuthal	$\Delta x = 3$ cm	$\theta = 0°$	$J_1^{(3)}$	0.417	0.418	82.09%	84.90%	66.56%
		$\theta = \pm 8°$	$J_4^{(3)}$	0.412	0.426	82.06%	79.24%	48.87%
	$\Delta x = 10$ cm	$\theta = 0°$	$J_4^{(3)}$	0.417	0.416	53.47%	33.96%	26.20%
		$\theta = \pm 40°$	$J_4^{(3)}$	0.422	0.425	38.52%	31.50%	24.74%
Rotation of the excitation port	$\varphi = 0°$		$J_1^{(4)}$	0.417	0.418	82.09%	84.90%	66.56%
	$\varphi = 30°$		$J_4^{(4)}$	0.418	0.421	72.87%	73.58%	57.81%
	$\varphi = 180°$		$J_4^{(4)}$	0.417	0.418	83.08%	75.47%	57.28%
Circular rotation of the Rx port	$\psi = 0°$		$J_4^{(5)}$	0.415	0.421	38.05%	22.81%	17.26%
	$\psi = \pm 30°$		$J_4^{(5)}$	0.415	0.423	33.32%	26.31%	18.75%
	$\psi = \pm 90°$		$J_1^{(5)}$	0.418	0.424	0%	20.67%	10.64%

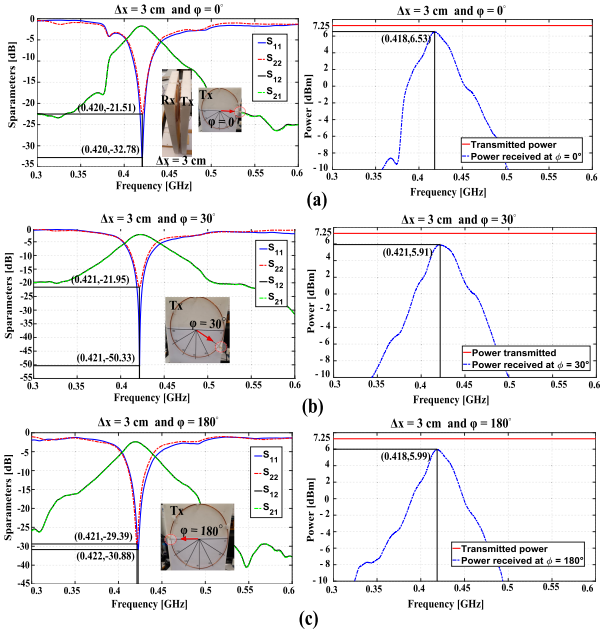

FIGURE 23. Measurements of the S-parameters (S_{11}, S_{22}, S_{21}, and S_{12}), and the PTE evaluation of the of the azimuthal misalignment configurations along: (a) Measurement setup; (b) $\Delta_x = 3$ cm and $\varphi = 0°$; (c) $\Delta_x = 3$ cm and $\varphi = 30°$; (d) $\Delta_x = 3$ cm and φ= 180°.

The rotation of the Tx port does not disrupt the power transmission phenomena; it is consistently maintained with a high efficiency.

E. MEASUREMENT OF THE ROTATIONAL MISALIGNMENT OF THE RX COIL

The last misalignment, depicted in Figs. 19(f) and 24, entails measuring the rotational positions of the Rx coil as it traces a circular path with a radius of 15 cm around the Tx coil. The CMA of this misalignment has revealed that certain positions exhibit identical behavior, but it did not yield substantial insights into power-related aspects.

The measured and calculated PTE values exhibit disparities, yet they demonstrate congruent variations. For instance, when the Rx coil is rotated by 30°, there is no discernible power loss in comparison to the initial configuration where both Tx and Rx coils are perfectly parallel. However, with a substantial 90° rotation, the calculated PTE becomes null, and the measured PETs reach their minimum values. Hence, in this particular setup, the calculated PTE displays heightened sensitivity in contrast to the measured values.

F. MAIN OBSERVATIONS: MEASUREMENTS OUTCOMES

Upon reviewing the simulated, computed and measured outcomes outlined in Table 4, several observations emerge. Initially, some discrepancies between calculated and measured PTEs may stem from different excitation techniques between simulations using FEKO software and experimental setups. Notably, FEKO integrates the excitation port directly within the antenna structure, while during measurements, excitation originates from the VNA via a coaxial cable. It is evident that coaxial cables have resistance, which causes power loss in the form of heat as current flows through the conductor. This resistance increases with cable length and frequency, leading to higher losses in longer cables. In essence, impedance mismatches, cable bending, or disparities in cable lengths can introduce additional power losses, resulting in reduced measured PTE. Within this study, the misalignment of coaxial cables interlinking the Tx and Rx

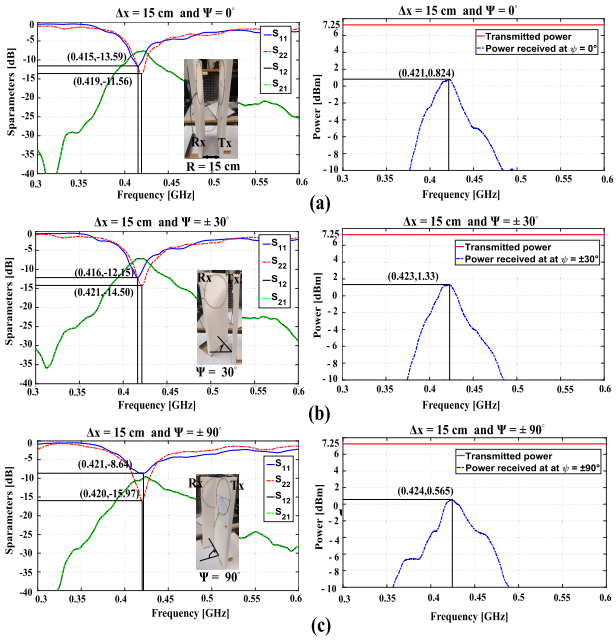

FIGURE 24. Measurements of the S-parameters (S_{11}, S_{22}, S_{21}, and S_{12}), and the PTE evaluation of the azimuthal misalignment configurations along: (a) Measurement setup; (b) $\Delta_x = 3$ cm and $\psi = 0°$; (c) $\Delta_x = 3$ cm and $\psi = 30°$; (d) $\Delta_x = 3$ cm and $\psi = 180°$.

loops with the VNA can exacerbate power dissipation during the measurement procedure of the WPT system, particularly under pronounced misalignment.

Furthermore, PTE was evaluated employing two distinct numerical expressions, each providing unique insights and resulting in divergent numerical outcomes. By definition, $PTE_{measured^2}$ and $PTE_{calculated}$ center on the transmission properties of the network, whereas $PTE_{measured^1}$ directly assesses the power delivery efficacy of the MCR-WPT system. As a result of comparing the measurement outcomes in Table 4, it is evident that $PTE_{measured^1}$ and $PTE_{measured^1}$ present different numerical values. Yet, the pivotal observation underscores that misalignment exerts a uniform impact on both calculated and measured PTE values, manifesting analogous variations that adhere to a consistent patterns. Adding to that, the comparison between measurements conducted with fabricated coils and simulation outcomes utilizing CMA confirms their efficacy in accurately forecasting the frequencies at which the maximum power transfer occurs across three scenarios. Notably, these frequencies align closely with the resonant frequencies of the dominant characteristic mode.

V. CONCLUSION

To the best of our knowledge, the main contribution presented in this investigation, which includes Characteristic Modes Analyses (CMA) in the field of Wireless Power Transmission have not been presented previously in the literature. Notably, measurements for various misalignment configurations between the transmitting (Tx) and the receiving (Rx) loops of Magnetically Coupled Resonant Wireless Power Transfer (MCR-WPT) system in real-world scenarios have been conducted.

Through establishing parallels between theoretical and experimental outcomes, the correlation between the Power Transfer Efficiency (PTE) and the resonant frequency (f_{res}) of the dominant mode becomes evident. Based on the various CMA established along this investigation, particularly through the examination of the contributions made by the distinct resonant Characteristic Modes (CMs) in the power level at the Rx loop and the intensity of their current distributions, it is evident that the Transmission Line Mode (TLM) J_4 consistently emerges as the mode exerting the most significant influence on the system behavior near its resonance.

The modal-coupling could be calculated through the application of the Coupled Mode Theory (CMT). Consequently, the resonant frequencies of the dominant TLM and its associated Antenna Mode (AM) play a key role in characterizing coupling phenomena. Based on the different analysis, the coupling effect between two loops vanishes when the TLM and its associated AM resonate at the same frequency of a single coil. In lateral and azimuthal misalignment scenarios, integrating the CMT was viable and practical. However, in rotational misalignments, CMs exhibited modal tracking behavior, rendering the application of CMT impractical. By elucidating the correlation between the attributes of CMs, focusing on the dominant Transmission Line Mode (TLM), J_4, this paper thoroughly outlines the observed frequency shift and Power Transfer Efficiency (PTE) across diverse scenarios with respect to theoretical and experimental perspectives.

Compared to lateral misalignments, rotational misalignments exert less impact on CMA of coupling and PTE of the system. Notably, symmetrical positions consistently exhibit uniform behavior in both CMA and measurements, offering potential for simplifying their analysis and measurement processes in future research.

Following this novel validation, CMA can be an effective tool in diminishing misalignment sensitivity and enhancing PTE through the application of selective excitation concepts. These concepts, previously successful in various literature applications, involve integrating capacitive and inductive loads to stimulate specific modes near their modal resonance. Within the realm of Wireless Power Transmission, the ideal CM displays a strong and consistent magnetic field between Tx and Rx units, along with a significant current distribution across the Rx loop.

REFERENCES

[1] H. Zhang, N. Shlezinger, F. Guidi, D. Dardari, M. F. Imani, and Y. C. Eldar, "Near-field wireless power transfer for 6G Internet of Everything mobile networks: Opportunities and challenges," *IEEE Commun. Mag.*, vol. 60, no. 3, pp. 12–18, Mar. 2022.

[2] B. Clerckx, Z. Popovic, and R. Murch, "Future networks with wireless power transfer and energy harvesting [scanning the issue]," *Proc. IEEE*, vol. 110, no. 1, pp. 3–7, Jan. 2022.

[3] J. Barreto, G. Perez, A.-S. Kaddour, and S. V. Georgakopoulos, "A study of wearable wireless power transfer systems on the human body," *IEEE Open J. Antennas Propag.*, vol. 2, pp. 86–94, 2021.

[4] M. S. Emara, M. Pisanello, L. Sileo, M. de Vittorio, and F. Pisanello, "A wireless head-mountable device with tapered optical fiber-coupled laser diode for light delivery in deep brain regions," *IEEE Trans. Biomed. Eng.*, vol. 66, no. 7, pp. 1996–2009, Jul. 2019.

[5] A. Sagar, A. Kashyap, M. A. Nasab, S. Padmanaban, M. Bertoluzzo, A. Kumar, and F. Blaabjerg, "A comprehensive review of the recent development of wireless power transfer technologies for electric vehicle charging systems," *IEEE Access*, vol. 11, pp. 83703–83751, 2023.

[6] Y. Wang, Z. Sun, Y. Guan, and D. Xu, "Overview of megahertz wireless power transfer," *Proc. IEEE*, vol. 111, no. 5, pp. 528–554, May 2023.

[7] M. Wagih, A. Komolafe, A. S. Weddell, and S. Beeby, "Broadband compact substrate-independent textile wearable antenna for simultaneous near- and far-field wireless power transmission," *IEEE Open J. Antennas Propag.*, vol. 3, pp. 398–411, 2022.

[8] H. Zhang, N. Shlezinger, F. Guidi, D. Dardari, and Y. C. Eldar, "6G wireless communications: From far-field beam steering to near-field beam focusing," *IEEE Commun. Mag.*, vol. 61, no. 4, pp. 72–77, Apr. 2023.

[9] V.-B. Vu, A. Ramezani, A. Triviño, J. M. González-González, N. B. Kadandani, M. Dahidah, V. Pickert, M. Narimani, and J. Aguado, "Operation of inductive charging systems under misalignment conditions: A review for electric vehicles," *IEEE Trans. Transport. Electrific.*, vol. 9, no. 1, pp. 1857–1887, Mar. 2023.

[10] Z. Yao, S. Luo, Z. Zhang, G. Li, X. Wei, X. Shen, N. Zhang, P. T. Krein, and H. Ma, "Analysis and design of multifrequency compensation strategy for wide misalignment tolerance in inductive power transfer systems," *IEEE Trans. Power Electron.*, vol. 38, no. 9, pp. 11705–11718, Sep. 2023.

[11] W. Su, Q. Zhang, S. Alkaraki, Y. Zhang, X.-Y. Zhang, and Y. Gao, "Radiation energy and mutual coupling evaluation for multimode MIMO antenna based on the theory of characteristic mode," *IEEE Trans. Antennas Propag.*, vol. 67, no. 1, pp. 74–84, Jan. 2019.

[12] P. Sumithra and D. Kannadassan, "Design and modeling of wideband planar antennas using characteristics modes," *IEEE Trans. Antennas Propag.*, vol. 69, no. 12, pp. 8257–8270, Dec. 2021.

[13] J.-F. Lin and L. Zhu, "Bandwidth and gain enhancement of patch antenna based on coupling analysis of characteristic modes," *IEEE Trans. Antennas Propag.*, vol. 68, no. 11, pp. 7275–7286, Nov. 2020.

[14] P. Liang and Q. Wu, "Characteristic mode analysis of antenna mutual coupling in the near field," *IEEE Trans. Antennas Propag.*, vol. 66, no. 7, pp. 3757–3762, Jul. 2018.

[15] J. J. Borchardt and T. C. Lapointe, "U-slot patch antenna principle and design methodology using characteristic mode analysis and coupled mode theory," *IEEE Access*, vol. 7, pp. 109375–109385, 2019.

[16] F. Abderrazak, E. Antonino-Daviu, L. Talbi, and M. Ferrando-Bataller, "Characteristic mode analysis of SCMR and CSCMR systems," in *Proc. 16th Eur. Conf. Antennas Propag. (EuCAP)*, Mar. 2022, pp. 1–5.

[17] A. A. Eteng, "Characteristic-mode analysis of coupled split-ring resonators," *J. Electr. Eng.*, vol. 73, no. 6, pp. 413–418, Dec. 2022.

[18] Q. Wu, W. Su, Z. Li, and D. Su, "Reduction in out-of-band antenna coupling using characteristic mode analysis," *IEEE Trans. Antennas Propag.*, vol. 64, no. 7, pp. 2732–2742, Jul. 2016.

[19] P. Liang, W. Su, and Q. Wu, "Characteristic mode analysis of near-field mutual coupling between wire and loop antennas," in *Proc. Asia–Pacific Int. Symp. Electromagn. Compat. (APEMC)*, vol. 1, May 2016, pp. 263–265.

[20] F. Abderrazak, E. Antonino-Daviu, M. Ferrando-Bataller, L. Talbi, and A. A. Qaraghuli, "A comparative study between different loop antennas topologies for wireless power transmission based on modal analysis," in *Proc. 15th Eur. Conf. Antennas Propag. (EuCAP)*, Mar. 2021, pp. 1–5.

[21] J. Gao, S. Tian, C. Yuan, Z. Ma, C. Gao, G. Yan, R. Li, Q. Tan, and L. Zhang, "Design and optimization of a novel double-layer Helmholtz coil for wirelessly powering a capsule robot," *IEEE Trans. Power Electron.*, vol. 39, no. 1, pp. 1826–1839, Jan. 2024.

[22] S. Jain, A. Bharadwaj, and A. Sharma, "Spatially arranged relay coils to improve the misalignment tolerance at an enhanced transfer distance," *IEEE Trans. Antennas Propag.*, vol. 72, no. 3, pp. 2171–2180, Mar. 2024.

[23] R. Harrington and J. Mautz, "Theory of characteristic modes for conducting bodies," *IEEE Trans. Antennas Propag.*, vol. AP-19, no. 5, pp. 622–628, Sep. 1971.

[24] R. Harrington and J. Mautz, "Computation of characteristic modes for conducting bodies," *IEEE Trans. Antennas Propag.*, vol. AP-19, no. 5, pp. 629–639, Sep. 1971.

[25] Z. Sun, G. Hu, Y. Wang, Y. Guan, and D. Xu, "Analysis and design of configurable rectifier with compensated near-zero impedance angle for megahertz wireless power transfer," *IEEE Trans. Ind. Electron.*, vol. 71, no. 5, pp. 4596–4606, Aug. 2024.

[26] M. Cabedo Fabrés, "Systematic design of antennas using the theory of characteristic modes," Ph.D. dissertation, Universitat Politècnica de València, 2008.

[27] M. Wang, J. Feng, Y. Shi, and M. Shen, "Demagnetization weakening and magnetic field concentration with ferrite core characterization for efficient wireless power transfer," *IEEE Trans. Ind. Electron.*, vol. 66, no. 3, pp. 1842–1851, Mar. 2019.

[28] Z. Luo and X. Wei, "Analysis of square and circular planar spiral coils in wireless power transfer system for electric vehicles," *IEEE Trans. Ind. Electron.*, vol. 65, no. 1, pp. 331–341, Jan. 2018.

[29] D. H. Nguyen, "Dynamic optical wireless power transfer for electric vehicles," *IEEE Access*, vol. 11, pp. 2787–2795, 2023.

[30] C. Liu, C. Jiang, J. Song, and K. T. Chau, "An effective sandwiched wireless power transfer system for charging implantable cardiac pacemaker," *IEEE Trans. Ind. Electron.*, vol. 66, no. 5, pp. 4108–4117, May 2019.

[31] F. Abderrazak, E. Antonino-Daviu, and M. Ferrando-Bataller, "Power transfer efficiency analyzed using characteristic mode coupling between two parallel loops," in *Proc. 14th Eur. Conf. Antennas Propag. (EuCAP)*, Mar. 2020, pp. 1–5.

[32] J.-S. Hong, "Couplings of asynchronously tuned coupled microwave resonators," *IEE Proc.-Microw., Antennas Propag.*, vol. 147, no. 5, p. 354, 2000.

[33] J. J. Borchardt, "Coupled and characteristic modes of a wideband slot antenna using FEKO," in *Proc. Int. Appl. Comput. Electromagn. Soc. Symp. (ACES)*, Aug. 2021, pp. 1–4.

[34] E. Safin and D. Manteuffel, "Advanced eigenvalue tracking of characteristic modes," *IEEE Trans. Antennas Propag.*, vol. 64, no. 7, pp. 2628–2636, Jul. 2016.

[35] D. Vital and S. Bhardwaj, "Misalignment resilient anchor-shaped antennas in near-field wireless power transfer using electric and magnetic coupling modes," *IEEE Trans. Antennas Propag.*, vol. 69, no. 5, pp. 2513–2521, May 2021.

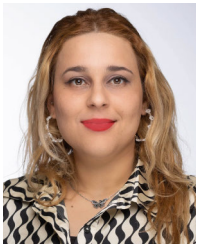

FERDAOUS ABDERRAZAK (Student Member, IEEE) was born in Kasr Hellal, Tunisia, in 1991. She received the bachelor's degree in industrial electronics engineering and the master's (By Research) degree in telecommunications engineering from the National Engineering School of Sousse (ENISO), Sousse, Tunisia, in 2016 and 2017, respectively. She is currently pursuing the dual Ph.D. degree with the Instituto de Telecomunicaciones y Aplicaciones Multimedia (iTEAM), Polytechnic University of Valencia (UPV), València, Spain, and in computer science and engineering with the Department of Computer Science and Engineering, University of Quebec in Outaouais, QC, Canada.

Her research interests include modal analysis and the design of antennas for biomedical and wireless applications. She has received various scholarships and awards. Notable among these are the mobility grant for students conducting their thesis under an international Cotutelle Agreement from the Vice-Rectorate of Research, Innovation, and Transfer with Universitat Politècnica de València, the Academic Perseverance Scholarships from La Fondation de l'UQO, and the Third Place Best Student Poster Award from STARaCom, McGill University, in June 2023.

EVA ANTONINO-DAVIU (Member, IEEE) was born in Valencia, Spain, in 1978. She received the M.S. and Ph.D. degrees in electrical engineering from the Universitat Politècnica de València, Valencia, Spain, in 2002 and 2008, respectively. In 2005, she joined the Communications Department, Universitat Politècnica de València, as an Assistant Professor, where she became an Associate Professor, in 2012. In 2005, she joined the Institute of Telecommunications and Multimedia Applications (iTEAM), where she became the Vice-Director of Research, in 2016. In 2005, she stayed as a Guest Researcher with the Department of Antennas & EM Modelling, IMST, Kamp-Lintfort, Germany; the Laboratory of Electronics, Antennas and Telecommunications (LEAT), University of Nice Sophia-Antipolis, France, in 2018; and the ATHENA Group, Georgia Institute of Technology, Atlanta, GA, USA, in 2019. She has published more than 200 papers in renowned journals and conferences in the field of antennas and propagation and two book chapters. Her current research interests include characteristic modes, small antennas, wideband and multi-band antenna design, antenna design for MIMO, the IoT, and mm-wave applications. She is an Associate Editor of *IEEE Antennas and Propagation Magazine*. Since 2018, she has been leading the EurAAP working Group on Small Antennas Eva Antonino and was a recipient of 2019 IEEE AP-S Lot Shafai Mid-Career Distinguished Achievement Award, for her contribution to the systematic design of antenna systems for practical applications using characteristic modes and promoting access of women to engineering.

LARBI TALBI (Senior Member, IEEE) received the M.S. and Ph.D. degrees in electrical engineering from Laval University, Quebec City, QC, Canada, in 1989 and 1994, respectively. He completed a Postdoctoral Fellowship with the Personal Communications Research Group, INR S-Telecommunications, Montreal, QC, Canada, from 1994 to 1995, where he led a project on wireless personal communication supported by Bell-Canada. From 1995 to 1998, he was an Assistant Professor with the Electronics Engineering Department, Riyadh College of Technology, Riyadh, Saudi Arabia. From 1998 to 1999, he was an Invited Professor with the Electrical and Computer Engineering Department, Laval University. He is currently a Full Professor with the Department of Computer Science and Engineering, University of Quebec in Outaouais, Gatineau, QC, Canada, where he joined, in 1999. In 2005, he spent his sabbatical leave, as an Invited Researcher with the Propagation Research (RVEP) Group, Satellite Communications and Radio Propagation Branch (VPSAT), Communication Research Center, Ottawa, ON, Canada. In 2006, he was a Visiting Professor with the Electrical and Electronics Engineering Department, Dumlupinar University, Kütahya, Turkey. He is currently leading two major projects on designing of new types of metasurfaces for reshaping the propagation channel environments. He has authored or coauthored over 200 journals and conference technical papers. His research interests include experimental characterization and modeling of millimeter-waves indoor radio propagation channels and design of antennas and microwave circuits for wireless communication systems. He was awarded the Best Paper Prize of IET-ICWCA Conference, in 2013, and recently, in March 2023, his team received a Best Paper Award for a work presented at iEECon, conference affiliated to IEEE. He is a member of the Order of Engineers of the Province of Quebec. He regularly acts as a reviewer of many international scientific journals and conferences and also for research funding organizations.

MIGUEL FERRANDO-BATALLER (Life Senior Member, IEEE) was born in Alcoy, Spain, in 1954. He received the M.Sc. (Ing.) and Ph.D. (Doctor) (Eng.) degrees in electrical engineering (telecommunication engineering) from the Technical University of Catalonia (UPC), Barcelona, Spain, in 1977 and 1982, respectively.

He has been a Research Assistant and an Associate Professor with the Antennas, Microwave, and Radar Group, Communications Department, Telecommunication Engineering School, UPC, in 1977 and 1982, respectively. In 1990, he joined the Universitat Politècnica de València (UPV), Valencia, Spain, where he is currently a Full Professor and the Leader of the Antenna and Propagation Laboratory. From 1991 to 1996, he was the Director of the Telecommunication Engineering School, UPV. From 1996 to 1999 and from 2005 to 2009, he was the UPV Vice-Rector of Academic Planning and Information and Communication Technologies. From 2009 to 2013, he was the Director of the Lifelong Learning Center, UPV. He has authored more than 200 technical articles, conference publications, and book chapters in specialized volumes. His current research interests include antennas, electromagnetic scattering, numerical methods, antenna design, and e-learning activities.